Available online at www.sciencedirect.com

jmr&t
Journal of Materials Research and Technology

journal homepage: www.elsevier.com/locate/jmrt

Effect of morphology and particle size on the electrical properties of nano-nickel ferrite

E.M. Kamar [a], *M. Khairy* [a,b,*], *M.A. Mousa* [a]

[a] *Chemistry Department, Faculty of Science, Benha University, Benha, Egypt*
[b] *Chemistry Department, College of Science, Imam Mohammad Ibn Saud Islamic University (IMSIU), Riyadh 11623, Saudi Arabia*

ARTICLE INFO

Article history:
Received 6 March 2023
Accepted 29 April 2023
Available online 5 May 2023

Keywords:
Nano
Morphology
$NiFe_2O_4$
Conductivity
Dielectric constant
Impedance

ABSTRACT

Four powder samples of Nickel ferrite ($NiFe_2O_4$) with different morphology and nanoparticle size have been synthesized by various methods: electrospinning, hydrothermal, green, and sol-gel. Through the use of XRD, FT-IR, SEM, TEM, and BET techniques, the prepared powders were characterized. The produced ferrite displayed a cubic spinel phase with various nanofiber, nanotube, nanorod, and nanosphere morphological structures. The electrical conductivity values for each sample increased with increasing temperature indicating the semiconducting behavior of all samples. The conductivity values were found to be dependent on each nanoparticle's size and morphology. The variation of dielectric constant (ε'), dielectric loss (ε''), and ac conductivity for the investigated samples at different temperatures and frequencies has been studied. Both dielectric constant (ε') and dielectric loss (ε'') were decreased with the increase of frequency while A.C. conductivity increased. Knop's phenomenological theory explains the frequency variation of (ε' and ε''). The hopping of electrons and holes is suggested to be the electrical conduction mechanism.

1. Introduction

It is recognized that the synthesis method is important, especially for the goal of material application. Moreover, a detailed description of particle size, shape, morphology, and crystallinity degree of material conduct to distinctive physical and chemical properties [1–4]. For nanostructured materials, the surface area to volume ratio is vast. The presence of available grain boundaries that dictate an unlimited density of defects has distinguished influences on the physical properties such as mechanical, electrical, electrochemical, and magnetic [5–12].

The nanoparticles possess a variety of shapes, and their names are characterized by their different shapes. For example, nanowires, nanorods, nanotubes, nanorings, nanospheres, nanoflakes, nanoflowers, nanobelts, etc. Controlling nanoparticles' morphology is crucial for exploiting their properties in several emerging technologies. Also, morphology variation is an effective way of controlling the functionality of nanomaterials because the variation of a large number of surface atoms with respect to their surface morphology determines their physical and chemical properties [13].

Compared with bulk counterparts, one-dimensional structures (nanotubes, nanorods, nanowires, etc.) that have surface effects, size effects, and macroscopic quantum tunneling effects offer prospects for enhancing the electrical, thermal, and mechanical properties of a broad range of functional materials [14–18] and play a meaningful role in the next generation of electron devices. Particularly, one-dimensional semiconductor nanowires have been envisioned as a candidate for efficient and

* Corresponding author.
E-mail address: mohkhairy@fsc.bu.edu.eg (M. Khairy).
https://doi.org/10.1016/j.jmrt.2023.04.266

small devices [19]. These devices may have a high packing density and be more efficient than microelectronic devices. The transport properties of these nanoscale device contacts are influenced by the charge carriers and the geometry of the semiconductor/metal interface [20]. Therefore, before incorporating nanoscale contacts into nanoscale electrical devices, the transport properties of these structures must be explored [21].

Spinel ferrites have gained much importance recently because of their interesting electrical and magnetic properties [22]. Usually, ferrite materials have low conductivity, and the order of magnitude of the conductivity greatly influences their dielectric and magnetic behavior [23]. Spinel ferrites are used in electronics and the telecommunication industry because of their navel electric properties, which make them useful in the radio-frequency circuit, high-quality factor, rod antennas, transformer cores, and read/write heads for high density, digital rapes [24,25]. The diversity of their applications originates from their considerable problems with crystal structure and electronic arrangements compared to other materials. Surface and quantum confinement phenomena are attributable to the enormous volume-to-surface ratio, and the scale-dependent characteristics of nano ferrites have received considerable attention. By varying such values, the desired changes in the physicochemical properties of the ferrites can be obtained [26–29].

Nickel ferrite ($NiFe_2O_4$) is one of the important spinel ferrites used for different technological applications due to its soft magnetic property, low eddy current loss, low conductivity, catalytic behavior, high electrochemical stability, abundance in nature, etc., [30,31]. $NiFe_2O_4$ exhibits an inverse spinel structure in which Fe^{3+} ions are equally distributed between octahedral B-sites and tetrahedral A-sites, whereas Ni^{2+} ions occupy only octahedral B-sites [32]. and exhibit the general formula $[Fe^{3+}\ ]_A[Ni^{2+}Fe^{3+}]_BO^{2-}{}_4$ [33]. On the other hand; the nano-nickel-ferrite is a mixed spinel ferrite with a cation distribution of $[Ni^{2+}Fe^{3+}]_A[\ Ni^{2+}\ Fe^{3+}]_B\ O^{2-}{}_4$ [34].

We previously reported the impact of synthetic methods and the morphological structure of nano $NiFe_2O_4$ on its electrical capacitance [35]. In the present work and based on the above discussion, we designed this work to explore the influence of particle size and morphology on the structural, dielectric dispersion, and electrical conductivity properties of the synthesized nanocrystalline $NiFe_2O_4$ ferrites prepared by different synthetic.

2. Experimental

2.1. Materials

All chemicals used were analytical-grade reagents and were used without any further purification. Deionized water was used through manifests in all the experiments. *Tamarindus indica* seeds were provided from the local market.

2.2. Synthetic methods

2.2.1. Preparation of $NiFe_2O_4$ nanofibers

Firstly, an electrospun precursor was organized by mixing a mixture of 30 mL of methanol, 1.5 g of PVP, 3.0 g of $Fe(NO_3)_3.9H_2O$, 3 mL of acetic acid, and 0.3 g of $Ni(CH_3COO)_2.4H_2O$, and magnetically stirred for 24 h at room temperature. Next, 6 mL of the gotten precursor was introduced into a 20 mL syringe with a 22 G stainless steel needle, joined to a high-voltage supply with a 20 kV applied voltage. The space between the needle end and the aluminum foil collector was 15 cm. The supply rate is adjusted to be 1.2 mL h^{-1} by a syringe pump. Lastly, the obtained spun fibrous were calcined at 825 K for 2 h (at a heating rate of 4 K min^{-1}) in a Muffle furnace under an air atmosphere. The sample obtained is denoted as NiF_f [35].

2.2.2. Preparation of $NiFe_2O_4$ nanotubes

Two grams of the as-synthesized sample NiF_f were placed in a 200 mL beaker filled with deionized water. After 4 h of high-speed magnetic stirring, the products were filtered and dried at 350 K for 24 h in a vacuum [35]. The sample is denoted as NiF_t.

2.2.3. Hydrothermal method (preparation of $NiFe_2O_4$ nanorods (NiF_{rd}))

Starting materials of 0.02 M $FeCl_3$ and 0.01 M $NiCl_2.6H_2O$ were dissolved in 200 mL of deionized water. Then 2.5 M NaOH solution was added dropwise until a pH of 1.5. After that, the suspended solution was transferred to a Pyrex flask (500 mL), which was sited inside an autoclave and heated at 435 K for 4 h under the stirring process. The suspended solution was washed thoroughly to release the formed salts and unreacted materials. The product was then filtered with filter papers and dried at 350 K in an oven for 4 h [35]. The sample was denoted as NiF_{rd}.

2.2.4. Green method

A green method was also used to prepare the $NiFe_2O_4$ sample by mixing *Tamarindus indica* seed powder and $Fe(NO_3)_3.9H_2O$ and $Ni(NO_3)_2.6H_2O$ with a molar ratio of 2:1 (Fe: Ni) in 60 mL deionized water. The ratio of metal nitrates to the seed powder is 1:1. The reaction mixture was heated with agitation in a microwave oven (frequency of 2.54 GHz at 900 W output power) for 30 min. The obtained product was annealed at 870 °C for 4 h [35]. The sample was denoted as NiF_s.

2.3. Characterizations

The samples were examined using a variety of methods, such as XRD, FT-IR, SEM, TEM, and BET, and the results obtained were discussed in detail in our previous work [35] and summarized in Table 1.

The electrical conductivity measurements were performed using a two–probe technique on pellets of 10 mm diameter and thickness of ~1 mm, prepared by pressing powder under a pressure of 2×10^3 kg/cm^2. The pellets were coated with silver paste, showing the sample's ohmic contact. The pellet was located in a sample holder inside a furnace and measured in the temperature range of 300–800 K. The dc-conductivity measurements were made using a Keithley 617 programmable electrometer. The ac-electrical measurements were performed at a constant voltage of 1 V and a frequency ranging from 10^3 to 10^6 Hz at 30 °C, using a precision LCR meter bridge (model HP 4284 A). The complex dielectric constant ε^{**} as a function of frequency is given by the well-known equation [36]:

Table 1 – XRD, T.E.M., FTIR, and N_2 adsorption data of the studied samples.

Sample	Synthetic method	D'_{XRD} [a] (nm)	Morphological Structure	$D^{\&}_{TEM}$ (nm)	ν_o [b] (cm^{-1})	ν_t [b] (cm^{-1})	Surface area (m^2/g)	Pore Size (nm)
NiF_f	electrospin	20	Fiber structure	Diam = 50-200 Length = several millimeters	451.3	562.5	360	6.1
NiF_t	Heating the NiF_f sample	33	Tube Structure	Diam. = 30 Length = 300	445.3	558.1	115	5.5
NiF_{rd}	hydrothermal	41	Rod Structure	Diam. = 35 Length = 100	444.3	556.4	82	4.7
NiF_s	Green method	50	Spherical Structure	–	443.9	556.2	54	4.1

[a] D'_{XRD} is particle size calculated from XRD using Scherrer s equation & D_{TEM} is Particle size using TEM.
[b] ν_1 and ν_2 are the tetrahedral and octahedral vibrations of Fe–O bonds in the spinel structure.

$$\varepsilon^{**}(\omega) = \varepsilon'(\omega) - j\varepsilon''(\omega) \quad (1)$$

where ε' and ε'' are the real and imaginary parts of the dielectric permittivity with $j = \sqrt{-1}$) and $\omega = 2\pi f$ is the frequency of the applied electric field. The values for ε' and ε'' were estimated using Eqs. (2) and (3) [36]:

$$\varepsilon' = Cd/\varepsilon^{o}A_s \quad (2)$$

$$\varepsilon''(\omega) = \varepsilon'(\omega)\tan\delta \quad (3)$$

where ε^{o} is the permittivity for free space ($\varepsilon^{o} = 8.86 \times 10^{-12}$ F/m), d is thickness, A_s is the cross-sectional area of the flat surface of the specimen, tan δ is a dissipative factor.

3. Results and discussion

3.1. Characterization

The XRD, SEM, TEM, and BET, previously published in our work [35] illustrated that all the synthesized samples exhibit spinel structure with a composition of $NiFe_2O_4$ and particle size and morphological structure (fibers, tubes, rods, and spheres) depending on the preparation method. The samples are denoted as NiF_f, NiF_t, NiF_{rd}, and NiF_s for fibers, tubes, rods, and spherical morphological structures. The main characteristic results are listed in Table 1 and supplementary Figs. (S1 and S2).

3.2. Electrical conductivity

3.2.1. Dc conductivity

Dc electrical conductivity (σ_{dc}) measurement is a powerful method to elucidate the electrical conductivity mechanism. At temperatures between 300 and 800 K, the relationship between temperature and the direct current conductivity (dc) of nickel ferrite samples is investigated. The produced data are displayed as the plots of ln $\sigma_{d.c}$ vs. 1/T, Fig. 1. It is noticed that there is a linear link between two areas that ends at Tc. This is the point at which the ferrimagnetic state transitions to the

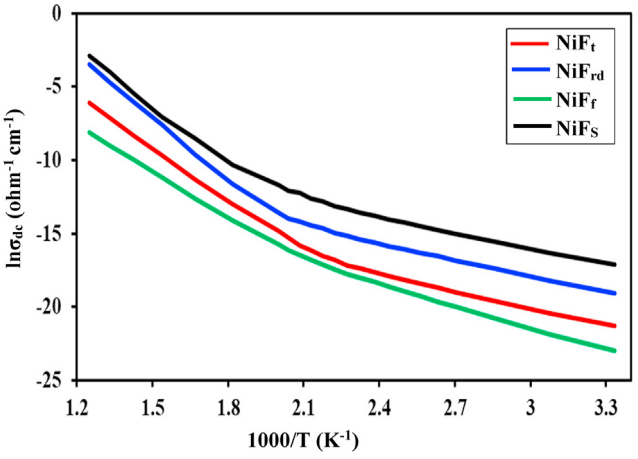

Fig. 1 – Effect of temperature on dc electrical conductivity of $NiFe_2O_4$ samples.

paramagnetic state. The change in Tc. With the variation in morphological structure can be explained by the A–B exchange interaction, which is dependent on the cation distribution between A and B-sites. The first region is ferrimagnetic and conducted via hopping (hopping conduction mechanism). The second region is a paramagnetic area that belongs to the disordered state. Each one of the different straight-line segments obeys the Arrhenius equation

$$\sigma_{dc} = \sigma_{o,dc} \exp(-E_{d.c} / kT) \quad (4)$$

where σ_o is a constant, $E_{d.c}$ is the activation energy, and k is the Boltzmann constant.

The dc-conductivity data of each sample were determined using the least-squares method and given in Table 2. The table illustrates that the samples are characterized by different electrical conductivity values depending on the morphological structure. At all temperatures investigated, the electrical conductivity value follows the order

$$NiF_s > NiF_{rd} > NiF_t > NiF_f$$

The conductivity data also show activation energy (E_{dc}) values ranging between 0.29 and 1.16 eV (depending on the measuring temperatures and the morphological structure). E_{dc} behaves similarly to conductivity. The sample with high conductivity exhibits low activation energy. The activation energy in the paramagnetic region is higher than the activation energy for the ferrimagnetic state), which indicates the influence of magnetic order on the conduction behavior. The conductivity and activation energies data point to a hopping conduction mechanism.

It was reported that in ferrite materials, the activation energy is frequently linked to the variant of the charge carrier mobility instead of charge concentration [37]. Therefore, the mobility of charge carriers is higher in the sample containing a spherical structure than in the other samples. Many authors [38–40] reported that the electrical conduction in ferrites arises from the electron hopping between cations of the same element in various valence states on similar lattice sites. For dc conductivity, the charge carriers select the easy-going track between ions, but these records may involve many hops for which the space between the ions is large. The conductivity of NiFrd and NiFt samples with rod and tube structures is greater than that of NiF_f samples with fibre structures; this can be attributed to conducting charge dispersions in rod-like particles [41].

3.2.2. *Ac conductivity*

Opposite to the Dc technique, which supports a total conductivity response of the material, ac technique differentiates between different mechanisms participating in the whole conductivity response of the material, such as the electrical conduction of grains and grain boundary as well as electrode response. The plots of ln σ_{ac} versus T^{-1}, at selected frequencies, are represented in Fig. 2. All the samples showed almost similar behavior with two slopes, in which the conductivity increased with temperature. The slopes at lower temperature ranges are higher than those at higher temperature ranges and obey for each range the relation:

$$\sigma_{ac} = \sigma_{o.ac} \exp(-E_{ac} / kT) \quad (5)$$

where $\sigma_{o,ac}$ is specific conductivity, and E_{ac} is the ac-activation energy.

The ac-conductivity data are summarized in Table 3. From which, it is noted that the ac conductivity decreases as the particle size decreases, which can be interpreted based on the intensification in grain boundary volume and the accompanying impedance to the flow of charge carriers [42,43]. On decreasing the particle size, the resistivity of the sample increases owing to increasing the number of grain boundaries than grains. At grain boundaries, there is an incompatibility between the energy states of neighboring grains and consequently work as hindrances to flowing the electrons.

The crystal structure of NiF_2O_4 is strongly influenced by the size of its particles, whereas the bulk $NiFe_2O_4$ exhibits an inverse spinel structure. Still, its small nanoscale nanometer has a mixed spinel structure [44]. Thus, the investigated samples are expected to have a mixed spinel structure with Ni^{2+} ions occupying both tetrahedral (A) and octahedral (B) sites. Accordingly, if the hopping frequency of the holes between $Ni^{2+} \leftrightarrow Ni^{3+}$ in tetrahedral sites is lesser than in octahedral sites, the conductivity is going to reduce with decreasing the particle size. This is because the number of Ni^{2+} filling tetrahedral sites will increase with the reduction in grain size [45].

Since the space between the cations present on B sites is smaller than the space between the cations occupied A sites; therefore, the intensity of covalency for the cations that occupy the A sites will be lower than that of the cations existing in B sites. Owing to these reasons, the mobility of the holes between Ni^{2+} and Ni^{3+} in the B sites is very high, with a smaller activation energy value than that in A sites. The conductivity at the B-sites owing to the holes is also

Table 2 – dc-electrical conductivity data of the studied samples.

Sample	Particle size[a](nm)	$\sigma_{dc} \times 10^{10}$ at 370 K	Temp. range (K)	E_{dc} (eV)
NiF_f	20	12.5	303–460	0.32
			460–800	0.87
NiF_t	33	34	303–420	0.41
			420–800	1.04
NiF_{rd}	41	298	303–490	0.31
			490–800	1.16
NiF_s	50	1800	303–450	0.29
			450–800	1.12

[a] Particle size calculated from XRD using Scherrer's equation.

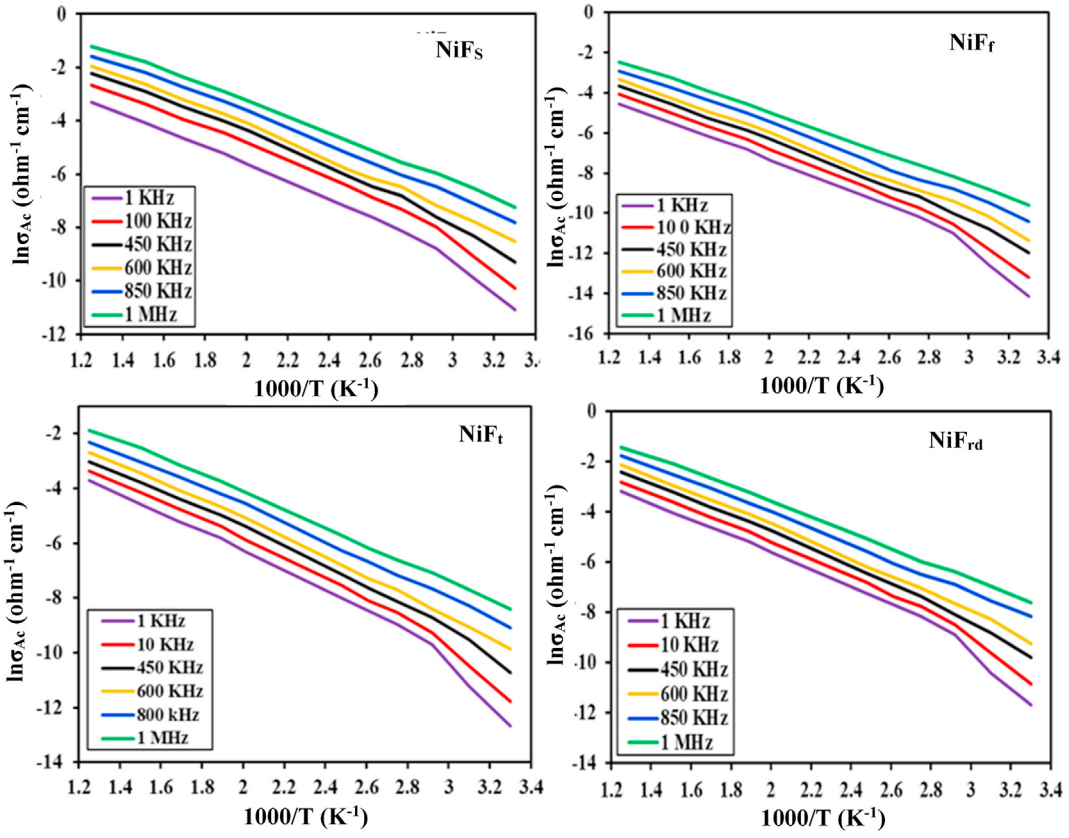

Fig. 2 – The effect of temperature on the Ac-electrical conductivity for the tested samples at some selected frequencies.

predictable only at lower temperatures than that of holes in the A-sites [46].

The effect of frequency on ac conductivity for the investigated specimens at some selected temperatures is shown in Fig. 3. The figure demonstrates that the ac conductivity rises with frequency, particularly at higher frequencies. The value of ac conductivity is greatest at higher frequencies due to the larger pumping force delivered to charge carriers by high frequency [47]. The enhancement in conductivity does not require that the number of charge carriers rises, but the

Table 3 – Electrical data of the $NiFe_2O_4$ samples.

Parameter	NiF_t	NiF_{rd}	NiF_f	NiF_s
σ_{dc} ($ohm^{-1}.cm^{-1}$) at 300 K	5.61×10^{-10}	5.17×10^{-9}	1.01×10^{-10}	3.70×10^{-8}
$E_{a,dc}$(eV), at (300–450 K)	0.32	0.31	0.42	0.30
σ_{dc} ($ohm^{-1}.cm^{-1}$), at 800 K	2.24×10^{-3}	2.21×10^{-2}	3.04×10^{-4}	3.5×10^{-2}
$E_{a,dc}$(eV), at (500–800 K)	0.99	1.16	0.87	1.0
σ_{ac} ($ohm^{-1}.cm^{-1}$), at (300 K, 1 kHz)	3.17×10^{-6}	8.44×10^{-6}	7.12×10^{-7}	1.54×10^{-5}
E_{ac}(eV), at (300–450 K, 1 kHz)	0.66	0.6	0.52	0.71
σ_{ac} ($ohm^{-1}.cm^{-1}$), at (300 K, 1 MHz)	2.25×10^{-4}	4.98×10^{-4}	6.94×10^{-5}	7.13×10^{-4}
E_{ac}(eV), at (450–800 K, 1 kHz)	0.37	0.31	0.28	0.28
σ_{ac} ($ohm^{-1}.cm^{-1}$), at (800 K, 1 kHz)	2.44×10^{-2}	4.15×10^{-2}	1.41×10^{-2}	3.7×10^{-2}
E_{ac}(eV), at (300–450 K, 1 MHz)	0.31	0.30	0.37	0.28
σ_{ac} ($ohm^{-1}.cm^{-1}$), at (800 K, 1 MHz)	1.51×10^{-1}	2.39×10^{-1}	8.38×10^{-1}	2.97×10^{-1}
E_{ac}(eV), at (450–800 K, 1 MHz)	0.27	0.25	0.23	0.23
τ (s)	2.3×10^{-12}	1.9×10^{-13}	7.8×10^{-13}	1.64×10^{-14}
E_τ (eV)	0.78	0.83	0.94	1.01
ε' at (300 K, 1 kHz)	3000	3570	2998	4517
ε' at (300 K, 1 MHz)	350	393	307	522
ε' at (800 K, 1 kHz)	2400	2900	2400	4414
ε' at (800 K, 1 MHz)	312	462	360	612
ε'' at (300 K, 1 kHz)	2100	2313	1829	3026
ε'' at (300 K, 1 MHz)	352	299	218	350
ε'' at (800 K, 1 kHz)	1920	2204	1703	2957
ε'' at (800 K, 1 MHz)	412	351	255	410

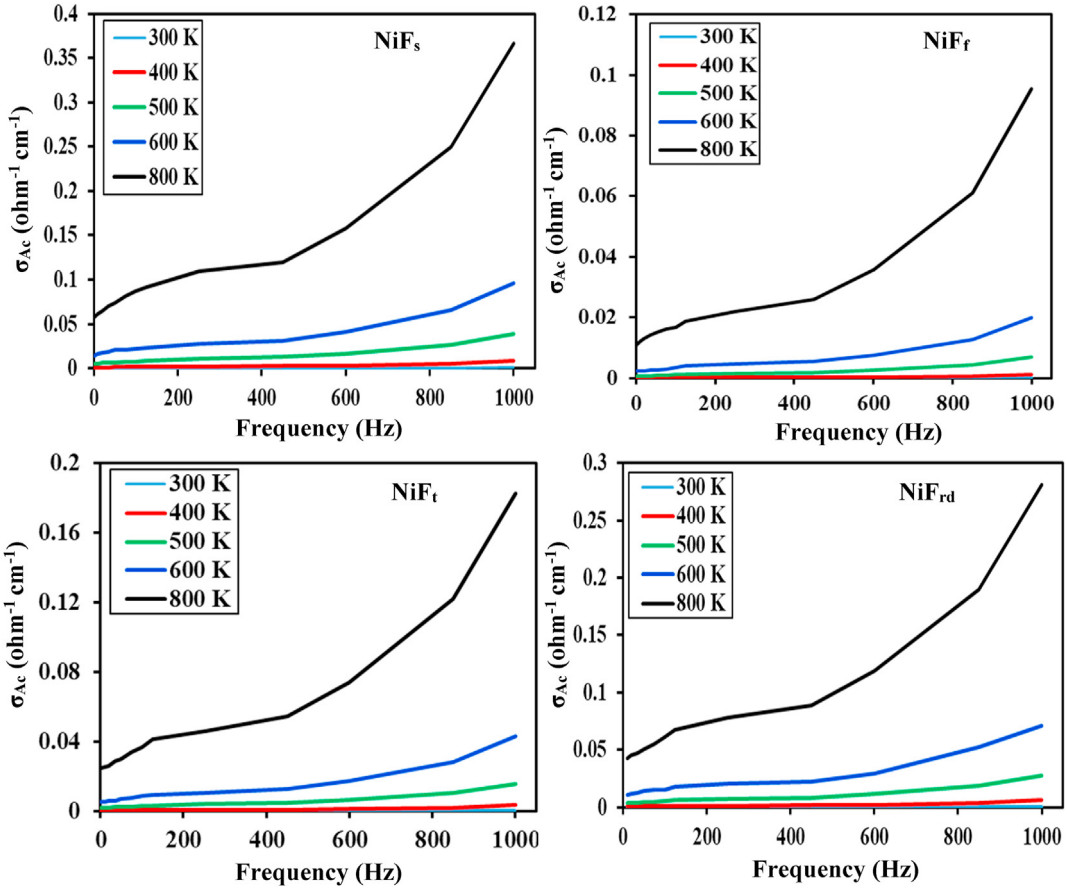

Fig. 3 – The effect of the frequency on Ac-electrical conductivity for the studied materials at selected temperatures.

hopping rate of charge between the charge carriers improves. The ac-conductivity data are summarized in Table 3.

The Koops model, which predicts that ferrite samples behave as a multilayer capacitor of grains and grain boundaries [48] might potentially explain the rise in ac conductivity with frequency and temperature. At lower frequencies, the resistive grain boundaries are more active, preventing electronic charge carriers from hopping between them, and a nearly continuous plateau area is observed. However, the conductive grains are more active at higher frequencies, allowing charge carriers to hop between neighboring ions.

Semiconductor materials have the following frequency-dependent relation

$$\sigma_{ac}(\omega) = A\omega^{s} \quad (6)$$

where A is a constant and $s \leq 1$. The phenomenon is attributed to the relaxation produced by the flow of electrons, tunneling or hopping, between the equilibrium sites [45]. The exponent s is calculated from plotting ln $\sigma_{a.c.}$ (ω) vs. ln (ω) and show values lie in the range of 0.041–0.087 and reduce with rising temperature, referring to that the correlated barrier hopping (C.B.H.) is the considerable plausible mechanism in the investigated samples [49].

Inspection of the conductivity data shows that the activation energy decreases as the frequency increases. As mentioned above, the charge carriers select the shortest track between the ions in the dc conductivity. These tracks will contain some jumps for which R, the space between the cations, is large, which is not so essential in the ac conduction. Consequently, small activation energy may be engaged in the ac conduction. The variance between the activation energies of σ_{dc} and σ_{ac} may be recognized as the valuable reduction in the electric field inner the bulk because of the presence of space charge collections at the electrodes, which were observed in dc-measurements [50,51].

3.3. *Dielectric properties*

3.3.1. *Dielectric constant behavior*

When a material is subjected to an external electric field, charge polarization stores some energy. The real component of the dielectric constant (ε′) represents this stored energy. The determination of dielectric constant is important for understanding the behavior of microstructural species such as grains and grain boundaries. The influence of frequency on the dielectric constant (ε′) of the studied samples at particular specified temperatures was drawn for this purpose, as shown in Fig. 4. The graph shows that ε′ decreases with increasing frequency for all samples. This decrease was rapid at lower frequencies and slower at higher frequencies. The concept of polarization and the hopping process can be used to understand the observed dielectric behavior [52]. The polarization in

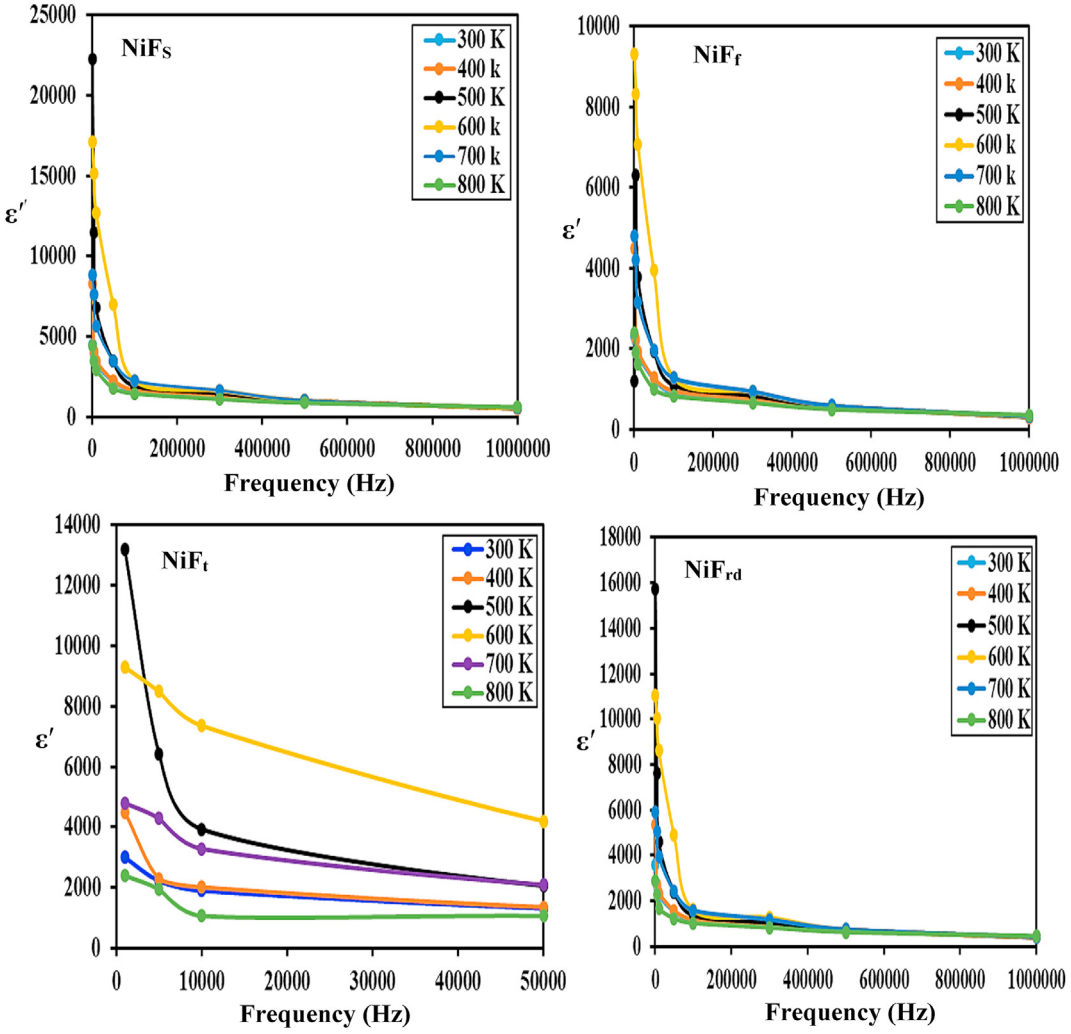

Fig. 4 – The effect of the frequency on the dielectric constant for the investigated samples at some selected temperatures.

our samples is attributed to electron hopping between $Fe^{2+} \leftrightarrow Fe^{3+}$ ions and hole hopping between $Ni^{3+} \leftrightarrow Ni^{2+}$ ions. Because our samples are presumed to be arranged of distinctive structures or regions (grain and grain boundaries) and the grain's conductivity is higher than the grain boundary. Therefore, it is appropriate to say that the higher ε' values are obtained from the charge accumulation at the grain boundaries [53]. Generally, According to the Koops, theory the interfacial polarization of the Maxwell-Wagner type can be used to analyze the dielectric dispersion curves [54,55]. These models predict that the ferrite crystal consists of conductor-rich grains separated by conductor-poor grain boundaries. The grain boundaries are more effective at low frequencies, whereas grains are more effective at higher frequencies. Ferrite materials are dipolar because of the abundance of Fe^{3+} ions and the relative rarity of Fe^{2+} ions. However, an ultrafine system has large numbers of grain boundaries and grains compared with the bulk case, which causes the phenomena to be more complex. Due to the large surface area of individual grains, nanomaterials also have an additional potential for demonstrating a high dielectric constant as a result of well-built surface polarization. Surface polarization plays a larger impact in determining the dielectric characteristics of ferrite materials in the low-frequency range than electronic or ionic polarization [56].

Our findings reveal that the dielectric constant of the examined materials rises with particle size: (at R.T. and 1 kHz, $\varepsilon' = 4517$, 3570, 3500, and 2998 for (NiFs (50 nm), NiF_{rd} (41 nm), NiF_t (33 nm), and NiF_f (20 nm), respectively. The dielectric constant variation trend with particle size contradicts the findings of Venkata et al. [57], which show that the dielectric constant increases with decreasing particle size. This disparity in data indicates that the dielectric constant is altered by particle size and potentially by morphological structural variation.

Fig. 5 illustrates the temperature dependence of ε' at several fixed frequencies. The results show an enhancement in ε' with increasing temperature to reach a maximum value before decreasing again. At lower temperatures, the change in ε' with temperature is weak. In narrowband semiconductors, the charge carriers are confined, producing polarization. Thus, the thermal energy provided to the samples at the lower

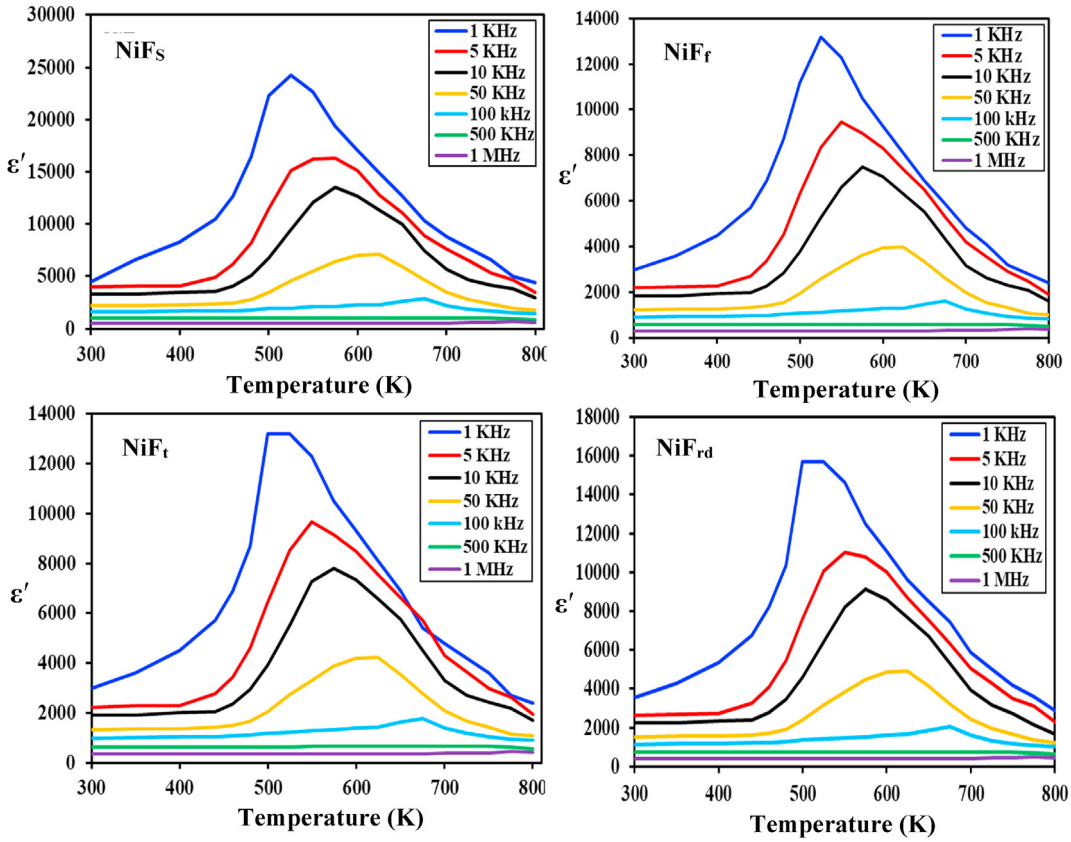

Fig. 5 – The effect of temperature on the dielectric constant for the investigated samples at some selected frequencies.

temperature range was insufficient to permit the localized dipoles to focus on the field direction. The number of charge carriers enlarges exponentially when higher temperatures are above the range in which ε' is slightly affected. Consequently, it creates more space charge polarization causing a rise in ε' to reach a maximum value and then reduces with increasing temperature. This can be clarified using the Rezlescu Model [58], which refers to the peaks in ε' (ω) curves produced from the collective donation of two various charge carriers to the polarization process. In our samples, the conduction process can be attributed to the presence of two types of charge carriers, that is, n-type owing to the hopping of electrons between Fe^{2+} and Fe^{3+}:

$$Fe^{3+} + e \leftrightarrow Fe^{2+}$$

As well as *p*-type, due to hopping of positive holes between the Ni ions:

$$Ni^{2+} + h \leftrightarrow Ni^{3+}$$

The obtained results also show that for all the samples, at each fixed temperature and frequency, ε' increases with enlarging the particle size of the $NiFe_2O_4$ sample. This is explained by the fact that minor grains denote slighter grain to grain surface contact area and then a lessened electron movement [59,60], consequently increasing their dielectric constant. As previously stated, we cannot rule out the potential of the morphological structure influencing the dielectric constant value. The observed ε'-values for the current nano-morphologies are as follows:

The ε'-values observed for the present nano-morphologies follow the order:

$$NiF_s > NiF_{rd} > NiF_t > NiF_f$$

The higher dielectric constant of the spherical particles than those of the other morphological structures look like the order of surface-to-volume ratios of the other morphologies, respectively. The same morphology-dependent behavior is reported for optical, surface plasmons, and catalytic activity [61–63].

3.3.2. *Dielectric loss behaviour*

Dielectric loss (ε'') represents dielectric absorption in a material. It is a parameter of a dielectric material that counts its inherent dissipation of electromagnetic energy at different frequencies. It measures the loss of electrical energy from the applied electric field into the samples at different frequencies. Figs. 6 and 7 depict the frequency and temperature dependence of dielectric loss (ε'') for all the samples. They demonstrated behavior similar to the dielectric constant and showed that, like the dielectric constant, dielectric loss correlates with particle size and morphological structure. The increased

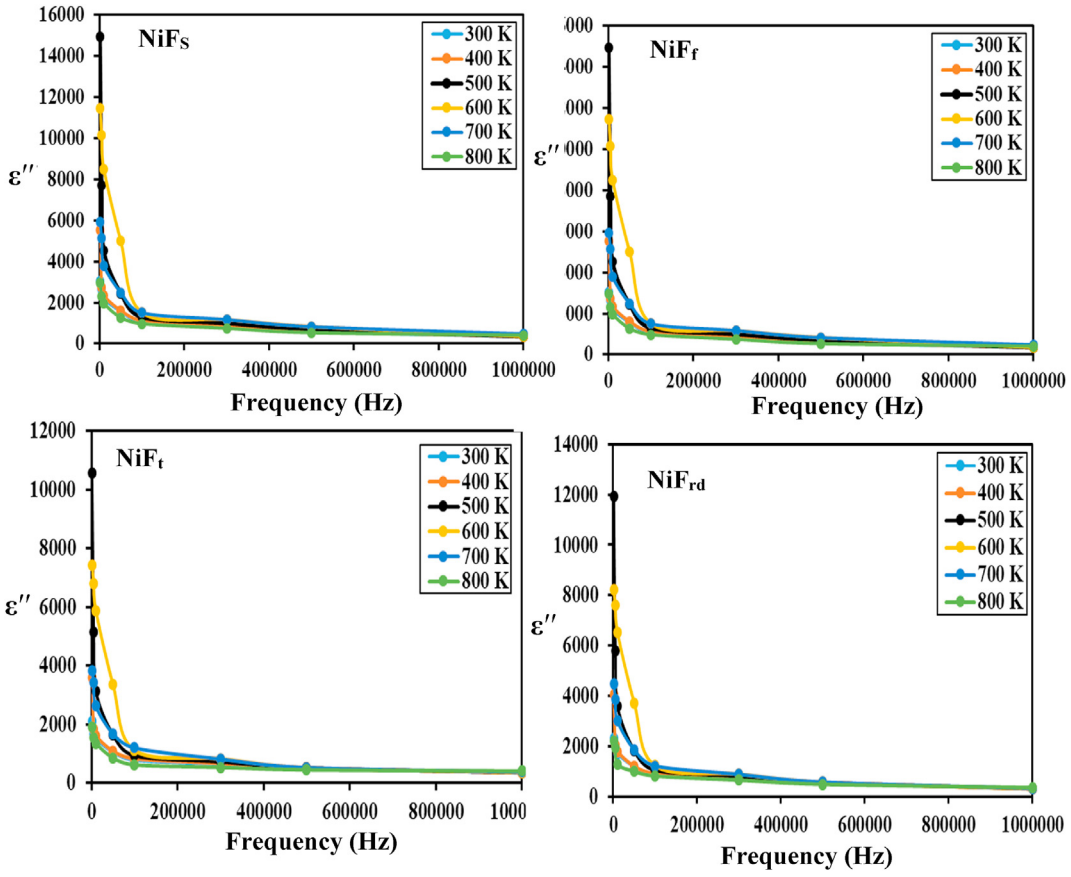

Fig. 6 – Frequency dependence of the dielectric loss for the investigated samples at some selected temperatures.

mobility of charge carriers causes the large energy losses observed in the low-frequency region. Charge carrier interactions with resistive grain boundaries are more common at low frequencies. Because dipoles realign themselves in response to the applied ac-field, values of ε" " are greater in the low-frequency zone. This might possibly be because the dipoles oppose each other during flipping, resulting in a loss of energy. Because charges cannot follow the applied ac-field at high frequencies, energy loss decreases due to the limited mobility of charges and their interaction with grain boundaries.

The results obtained, Fig. 7, show that dielectric loss exhibits a peaking nature in ε″- T plots for all the different morphological structures, and slight shifts in these maxima are detected. The situation for having a maximum in ε″ of dielectric material is presented by the relation [64].

$$\omega\tau = 1 \tag{7}$$

where ω is the angular frequency and τ is the relaxation time. The maximum dielectric loss is obtained when the applied frequency of the electric field turns out to be approximately equal to the hopping frequency of electrons among both ionic sites [65].

The increase in charge carrier hopping frequency with temperature is what causes the maxima of ε″ curves to move with temperature to higher frequencies. The relaxation period in this instance can be written as [45]:

$$\tau = \tau_o \, e \, E_\tau / (kT) \tag{8}$$

where E is the activation energy for dielectric relaxation, k is the Boltzmann constant, and τ_o is the relaxation duration at an infinitely high temperature. For the samples under investigation, the plots of ln τ vs $10^3/T$ displayed straight lines, from which E_τ was calculated and listed in Table 3, which showed E_τ –values lie between 0.78 and 1.01 eV and follow the following order:

$$NiF_s > NiF_f > NiF_{rd} > NiF_t$$

Generally, our data showed that the dielectric data varies fundamentally with the variation in each of the morphological structures and porosity of the samples. It was reported that dielectric losses decrease with increasing porosity, as shown in our results [66]. Introducing porosity into material changes its qualities, such as heat conductivity and mechanical or electrical properties. Porosity can behave in various ways based on the volume fraction of porosity, pore size, pore size distribution, pore shape, and interconnectivity. However, it is difficult to explain in what percentage each morphological structure, microstructure defects such as grain boundaries, insulating inclusions, or fractures is responsible for the observed effect [67].

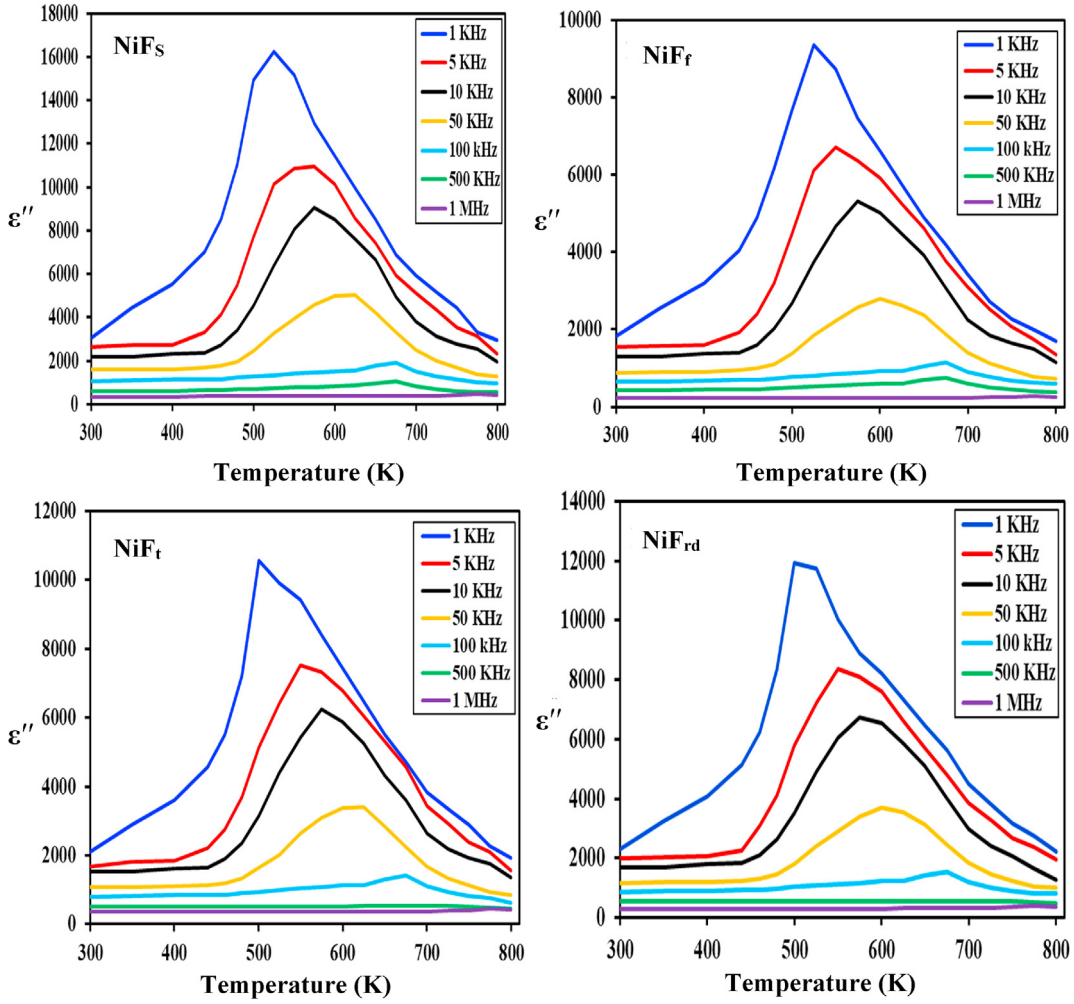

Fig. 7 – Temperature dependence of dielectric loss for the investigated samples at some selected frequencies.

3.4. *Impedance spectroscopy*

Impedance spectroscopy (EIS) is a common and effective practical approach that provides details about the electrical processes occurring inside samples and their relationships to the samples' microstructure, grains, and grain boundary effects [66].Generally, the Nyquist impedance plot shows two separating semicircles, the left semicircle represents the grain resistance, and the right one represents the grain boundary, and they possess different relaxation times. When the relaxation time ratio of the two processes is less than a hundred, the two semicircles will overlap. Fig. 8 demonstrates the Nyquist plots of the investigated samples. Each sample exhibits a single semicircle arc from lower frequency to higher frequency, proposing enhanced grain-boundary effects within the samples. Additionally, the Nyquist plots show partial semicircles and not full semicircles. Moreover, it is found that the centers of semicircles lie below the abscissa (Z′) axis, which suggests the dielectric relaxation is of non-Debye type in all the samples [68]. The diameters of the semicircle are 3.74×10^6, 4.05×10^6, 4.24×10^6, and 4.57×10^6 Ω, for NiF_s, NiF_{rd}, NiF_t, and NiF_t, respectively, which are distinctive for different samples because of the difference in the resistance of the ferrite samples [69,70].

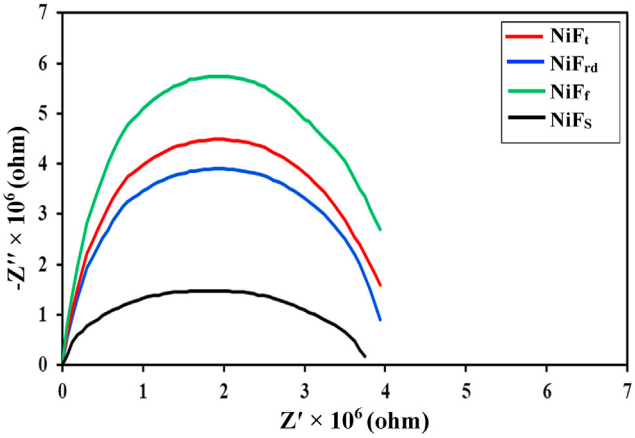

Fig. 8 – Cole-Cole diagram for the investigated samples at room temperature.

4. Conclusion

Reported results have shed light on the effect of particle size and the morphological structure on the electrical properties of the $NiFe_2O_4$ nanoparticles. The present work studied the electrical properties of four nano-$NiFe_2O_4$ samples with different morphological structures of a tube, rod, fiber, and sphere were studied. At various temperatures and frequencies, the dielectric constant and ac-electrical conductivity were measured. The dc-electrical conductivity of all samples increased with increasing temperature referring to semiconducting behavior. The dc-conductivity increased with increasing the particle size in the order of $NiF_s > NiF_t > NiF_{rd} > NiF_f$. Morphology variation causes a variation in both the band gap and the electrical conductivity values, especially at higher temperatures. Such properties could find applications in recording, storage memory devices, optical devices, and military applications. The a.c electrical conductivity of all samples increased with increasing frequency in a manner that is explained based on the hopping mechanism. The conduction process was interpreted based on the existence of two types of charge carriers, that is, n-type due to the hopping of electrons between Fe^{2+} and Fe^{3+} ions and hopping of positive holes between Ni^{2+} and Ni^{3+}. The influence of frequency on each dielectric constant ε, and the dielectric loss ε''showed maximum value at a certain frequency for all the morphological structures. Typical dielectric dispersion nature is observed at lower frequencies, which was successfully interpreted on the basis of the Maxwell-Wagner'sgner theory of interfacial polarization in consonance with the Koops phenomenological theory. This behavior is clarified qualitatively in terms of the assumption that the mechanism of the polarization process is electronic polarization. The dielectric constant for all samples is very high. They have values of 2998, 3000, 3570, and 4517 at room temperature for NiF_f, NiF_t, NiF_{rd}, and NiF_s, respectively, demonstrating the possibility of their potential application in dielectric supercapacitors. The complex impedance analysis verifies the predominant contribution of grain boundary in the conduction mechanism at high frequencies. The high ac conductivity and low dielectric loss recorded for all examined samples at high frequencies indicate that these samples are suitable for high-frequency power transformer applications. Future research would continue to study the impact of morphology on magnetic storage devices and medical sensors and its applications in various medical fields, such as antibacterial agents, immunoassays, hyperthermia therapy, and magnetic resonance imaging.

Declaration of competing interest

The authors declare that they have no known competing financial interests or personal relationships that could have appeared to influence the work reported in this paper.

Appendix A. Supplementary data

Supplementary data to this article can be found online at https://doi.org/10.1016/j.jmrt.2023.04.266.

REFERENCES

[1] Nahirniak S, Dontsova T, Dusheiko M, Smertenko P, Kwapinski W. Effect of SnO_2 structure morphology on their electrical properties. J Mater Sci Mater Electron 2020;31:21934–47.

[2] Periyasamy M, Kar A. Modulating the properties of SnO_2 nanocrystals: morphological effects on structural, photoluminescence, photocatalytic, electrochemical and gas sensing properties. J Mater Chem C 2020;8:4604–35.

[3] Makeswaran N, Battu AK, Deemer E, Ramana CV. Crystal growth and structure–property optimization of thermally annealed nanocrystalline Ga_2O_3 films. Cryst Growth Des 2020;20:2893–903.

[4] Jiang SP. Nanoscale and nano-structured electrodes of solid oxide fuel cells by infiltration: advances and challenges. Int J Hydrogen Energy 2012;37:449–70.

[5] Jeevanandam J, Barhoum A, Chan YS, Dufresne A, Danquah MK. Review on nanoparticles and nanostructured materials: history, sources, toxicity and regulations. Beilstein J Nanotechnol 2018;9:1050–74.

[6] Chen X, Shi T, Zhong K, Wu G, Lu Y. Capacitive behavior of MoS_2 decorated with FeS_2@carbon nanospheres. Chem Eng J 2020;379:122240.

[7] Wu H, Wu G, Wang L. Peculiar porous α-Fe_2O_3, γ-Fe_2O_3 and Fe_3O_4 nanospheres: facile synthesis and electromagnetic properties. Powder Technol 2015;269:443–51.

[8] Chakraverty AP, Dash S, Maharana HS, Beura S, Mohanty UK. A novel investigation on durability of GRE composite pipe for prolonged sea water transportation. Compos Commun 2020;17:42–50.

[9] Zhou X, Jia Z, Feng A, Qua S, Wang X, Liu X, et al. Synthesis of porous carbon embedded with NiCo/$CoNiO_2$ hybrids composites for excellent electromagnetic wave absorption performance. J Colloid Interface Sci 2020;575:130–9.

[10] Wu G, Zhang H, Luo X, Yang L, Lv H. Investigation and optimization of Fe/$ZnFe_2O_4$ as a Wide-band electromagnetic absorber. J Colloid Interface Sci 2019;536:548–55.

[11] Lv H, Zhou X, Wu G, Kara U, Wang X. Engineering defects in 2D g-C_3N_4 for wideband, efficient electromagnetic absorption at elevated temperature. J Mater Chem 2021;9:19710–8.

[12] Zhou X, Wang B, Jia Z, Zhang X, Liu X, Wang K, et al. Dielectric behavior of Fe_3N@C composites with green synthesis and their remarkable electromagnetic wave absorption performance. J Colloid Interface Sci 2021;582:515–25.

[13] Thomas P, Jose AJ. Chapter: dependence of morphology on optical and electrical properties of metal oxide nanostructures. In: Applied chemistry and chemical engineering. 1st Ed. Apple Academic Press; 2018.

[14] Lei D, Benson J, Magasinski A, Berdichevsky G, Yushin G. Transformation of bulk alloys to oxide nanowires. Science 2017;355:267–71.

[15] Ali SS, Li WJ, Javed K, Shi DW, Riaz S, Zhai GJ, et al. Exchange bias in two-step artificially grown one-dimensional hybrid Co-$BiFeO_3$ core-shell nanostructures. Nanotechnology 2016;27:045708.

[16] Lei Y, Zeng HZ, Luo WB, Shuai Y, Wei XH, Du N, et al. Ferroelectric and flexible barrier resistive switching of epitaxial $BiFeO_3$ films studied by temperature-dependent current and capacitance spectroscopy. J Mater Sci Mater Electron 2016;27:7927–32.

[17] Prashanthi K, Dhandharia P, Miriyala N, Gaikwad R, Barlage D, Thundat T. Enhanced photo-collection in single $BiFeO_3$ nanowire due to carrier separation from radial surface field. Nano Energy 2015;13:240–8.

[18] Chybczyńska K, Markiewicz E, Błaszyk M, Hilczer B, Andrzejewski B. Dielectric response and electric conductivity

of ceramics obtained from $BiFeO_3$ synthesized by microwave hydrothermal method. J Alloys Compd 2016;671:493–501.
[19] Yu P, Wu J, Liu S, Xiong J, Jagadish C, Wang ZM. Design and fabrication of silicon nanowires towards efficient solar cells. Nano Today 2016;11:704–37.
[20] Lavieville R, Zhang Y, Casu A, Genovese A, Manna L, Di Fabrizio E, et al. Charge transport in nanoscale "all-inorganic" networks of semiconductor nanorods linked by metal domains. ACS Nano 2012;6:2940–7.
[21] Chen S, Griffin PB, Plummer JD. Negative differential resistance circuit design and memory applications. IEEE Trans Electron Dev 2009;56:634–40.
[22] Reddy PV, Rao TS. Dielectric behaviour of mixed Li-Ni ferrites at low frequencies. J Less Common Met 1982;86:255–61.
[23] Ahmed MA. Electrical properties of Co-Zn ferrites. Phys Status Solidi A 1989;111:567–72.
[24] Vinosha PA, Manikandan A, Preetha AC, Dinesh A, Slimani Y, Almessiere MA, et al. Review on recent advances of synthesis, magnetic properties, and water treatment applications of cobalt ferrite nanoparticles and nanocomposites. J Supercond Nov Magnetism 2021;34:995–1018.
[25] Valenzuela R. Novel applications of ferrites. Physiother Res Int 2012;2012. https://doi.org/10.1155/2012/5918.
[26] Maha M, Oday S, Ahmed MH, Samir AAK, Ryad G, Osama MH, et al. Structure, morphology and electrical/magnetic properties of Ni-Mg nano-ferrites from a new perspective. Nanomaterials 2022;12:1045.
[27] Ibtihel S, Khawla BB, Abderrazek O, Abdelhedi A, Kamel K, Benali A, et al. Research on the physical properties of $LiMn_{0.5}Fe_2O_4$ spinel ferrites by the combination of optical, magnetic, and dielectric behaviors. RSC Adv 2023;13:9260–72.
[28] Deraz NM. Glycine-assisted fabrication of nanocrystalline cobalt ferrite system. J Anal Appl Pyrolysis 2010;88:103–9.
[29] Deraz NM. Size and crystallinity-dependent magnetic properties of copper ferrite nano-particles. J Alloys Compd 2010;501:317–25.
[30] Ruthradevi T, Akbar J, Kumar GS, Thamizhavel A, Kumar G, Vatsa R, et al. Investigations on nickel ferrite embedded calcium phosphate nanoparticles for biomedical applications. J Alloys Compd 2017;695:3211–9.
[31] Gunjakar JL, More AM, Gurav KV, Lokhande CD. Chemical synthesis of spinel nickel ferrite ($NiFe_2O_4$) nano-sheets. Appl Surf Sci 2008;254:5844–8.
[32] Tan J, Zhang W, Xia A-L. Facile synthesis of inverse spinel $NiFe_2O_4$ nanocrystals and their superparamagnetic properties. Mater Res 2013;16(1):237–41.
[33] Goldman A. Modern ferrite technology. New York: Marcel Dekker; 1993.
[34] Atif M, Nadeem M, Siddique M. Cation distribution and enhanced surface effects on the temperature dependent magnetization of as-prepared $NiFe_2O_4$ nanoparticles. Appl Phys A 2015;120:571–8.
[35] Toghan A, Khairy M, Kamar EM, Mousa MA. Effect of particle size and morphological structure on the physical properties of $NiFe_2O_4$ for supercapacitor application. J Mater Res Technol 2022;19:3521–35.
[36] Mlsra DK. Evaluation of the complex permittivity of layered dielectric materials with the use of an open-ended coaxial line. Microw Opt Technol Lett 1996;137:183–7.
[37] Ashok A, Somaiah T, Ravinder D, Venkateshwarlu C, Reddy CS, Rao KN, et al. Electrical properties of cadmium substitution in nickel ferrites. World J Condens Matter Phys 2012;2:257–66.
[38] Sigamani M, Manja KS. Ac electrical conductivity and dielectric behavior of nanophase nickel ferrites. J Alloys Compd 2008;457(1):522–5.
[39] Iqbal MJ, Ahmad Z, Meydan T, Melikhov Y. Physical, electrical and magnetic properties of nano-sized Co-Cr substituted magnesium ferrites. J Appl Phys 2012;111:033906.
[40] Aravind G, Ravinder D, Nathanial V. Structural and electrical properties of Li–Ni nanoferrites synthesised by citrate gel autocombustion method. Physiother Res Int 2014;2014:11. https://doi.org/10.1155/2014/672739. 672739.
[41] Majidian M, Grimaldi C, Forró L, Magrez A. Role of the particle size polydispersity in the electrical conductivity of carbon nanotube epoxy, Composites. Sci Rep 2017;7:12553.
[42] Satyavani TVSL, Kiran BR, Kumar VR, Kumar AS, Naidu SV. Effect of particle size on dc conductivity, activation energy and diffusion coefficient of lithium iron phosphate in Li-ion cells. Eng Sci Technol Int J 2016;19:40–4.
[43] Ghosh P, Bhowmik RN, Bandyopadhyay S, Mitra P. Influence of particle size on the electrical properties and magnetic field dependent I–V characteristics of nanocrystalline ZnFe2O4. Trans Indian Ceram Soc 2019;78:111–20.
[44] Jacob J, Abdul Khadar M. Investigation of mixed spinel structure of nanostructured nickel ferrite. J Appl Phys 2010;107:114310.
[45] Ghatak S, Sinha M, Meikap AK, Pradhan SK. Anomalous electrical transport properties of nonstoichiometric nickel ferrite below room temperature. Mater Res Bull 2011;46(7):1055–64.
[46] Ajmal M, Maqsood A. Influence of zinc substitution on structural and electrical properties of $Ni_{1-x}Zn_xFe_2O_4$ ferrites. Mater Sci Eng B 2007;139(2–3):164–70.
[47] Rao BP, Rao KH. Effect of sintering conditions on resistivity and dielectric properties of Ni-Zn ferrites. J Mater Sci 1997;32:6049–54.
[48] Sivakumar D, Naidu KCB, Nazeer KP, Raf MM, Rameshkumar G, Sathyaseelan B, et al. Structural characterization and dielectric properties of superparamagnetic iron oxide nanoparticles. J Korean Ceram Soc 2018;55:230–8.
[49] Mohammed MI, Abd – Allah Kh, Hassaan MY. The conduction mechanism and dielectric behavior of sodium borate glasses containing Fe and Bi ions. Egypt J Solid 2004;27(2):299–308.
[50] Elliott SR. Frequency-dependent conductivity in ionic glasses: a possible model. Solid State Ionics 1988;27:131–49.
[51] Assim EM, El-Metwally EG, Abdel-Aziz MM. Electrical and dielectric properties of amorphous GeTe alloy. Eur Phys J B 2019;92:276.
[52] Kambale RC, Shaikh PA, Bhosale CH, Rajpure KY, Kolekar YD. Dielectric properties and complex impedance spectroscopy studies of mixed Ni–Co ferrites. Smart Mater Struct 2009;18:085014.
[53] Bhat I, Husain S, Khan W, Patil SI. Structural, transport, magnetic, and dielectric properties of [La1-x][Tex]MnO3 (x = 0.10 and 0.15). J Mater Sci 2013;48:3272–82.
[54] Melagiriyappa E, Jayanna HS, Chougule BK. Dielectric behavior and ac electrical conductivity study of Sm^{3+} substituted Mg-Zn ferrites. Mater Chem Phys 2008;112:68–73.
[55] Mondal RA, Murty BS, Murthy VRK. Maxwell–Wagner polarization in grain boundary segregated NiCuZn ferrite. Curr Appl Phys 2014;14(12):1727–33.
[56] Kumar KV, Lakshmi M, Thyagarajan K, Krishna KR. Composition and frequency dependent dielectric properties of Cr-Co nano ferrites. Asian J Phys Chem Sci 2017;4(2):1–9.
[57] Parashar SKS, Choudhary RNP, Murty BS. Size effect of Pb0.92Nd0.08(Zr0.53Ti0.47)0.98O3 nanoceramic synthesized by high-energy ball milling. J Appl Phys 2005;98:104305.
[58] Mazen SA, Abu-Elsaad NI. Structural, magnetic and electrical properties of the lithium ferrite obtained by ball milling and heat treatment. Appl Nanosci 2015;5:105–14.
[59] Kuezynski GC, Hooton NA, Gibbon CF. Sintering and related phenomenon. New York: Gordon and Breach; 1967. p. 65.

[60] Lv L, Zhou J-P, Liu Q, Zhu G, Chen X-Z, Bian X-B, et al. Grain size effect on the dielectric and magnetic properties of $NiFe_2O_4$ ceramics. Phys E: Low-Dimens Syst Nanostruct 2011;43:1798–803.
[61] Leong ESP, Liu YJ, Wang B, Teng J. Effect of surface morphology on the optical properties in metal dielectric metal thin film systems. ACS Appl Mater Interfaces 2011;3:1148–53.
[62] Li J, Du B, Wang F, Yao W, Yao S. The effect of nanoparticle surfactant polarization on trapping depth of vegetable insulating oil-based nanofluids. Phys Lett 2016;380:604–8.
[63] Zahn Z, Wang W, Ninghua N, Sun S, Qinghua Q, Liang L, et al. Morphology effects on space charge characteristics of low density polyethylene. Jpn J Appl Phys 2011;50:017101.
[64] Ktitorov SA. Determination of the relaxation time distribution function from dielectric losses. Tech Phys Lett 2003;29:956–8.
[65] Varshney D, Verma K. Substitutional effect on structural and magnetic properties of $A_xCo_{1-x}Fe_2O_4$ (A = Zn, Mg and x = 0.0, 0.5) ferrites. J Mol Struct 2011;1006:447–52.
[66] Upadhyay C, Verma HC, Anand S. Cation distribution in nanosized Ni-Zn ferrites. J Appl Phys 2004;95:5746–51.
[67] Pérez-Coll D, Sánchez-López E, Mather GC. Influence of porosity on the bulk and grain boundary electrical properties of Gd-doped ceria. Solid State Ionics 2010;181:1033–42.
[68] Almessiere MA, Slimani Y, Sayed HSEI, Baykal A. Morphology and magnetic traits of strontium nanohexaferrites: effects of manganese/yttrium co-substitution. J Rare Earths 2019;37:739–40.
[69] Gul IH, Pervaiz E. Comparative study of $NiFe_{2-x}Al_xO_4$ ferrite nanoparticles synthesized by chemical co-precipitation and sol-gel combustion techniques. Mater Res Bull 2012;47(6):1353–61.
[70] Ramesh B, Ramesh S, Kumar RV, Lakshmipathi RM. AC impedance studies on $LiFe_{5-x}Mn_xO_8$ ferrites. J Alloys Comps 2012;513:289–93.